



# Ball-milled bismuth oxychloride/biochar nanocomposites with rich oxygen vacancies for reactive red-120 adsorption in aqueous solution

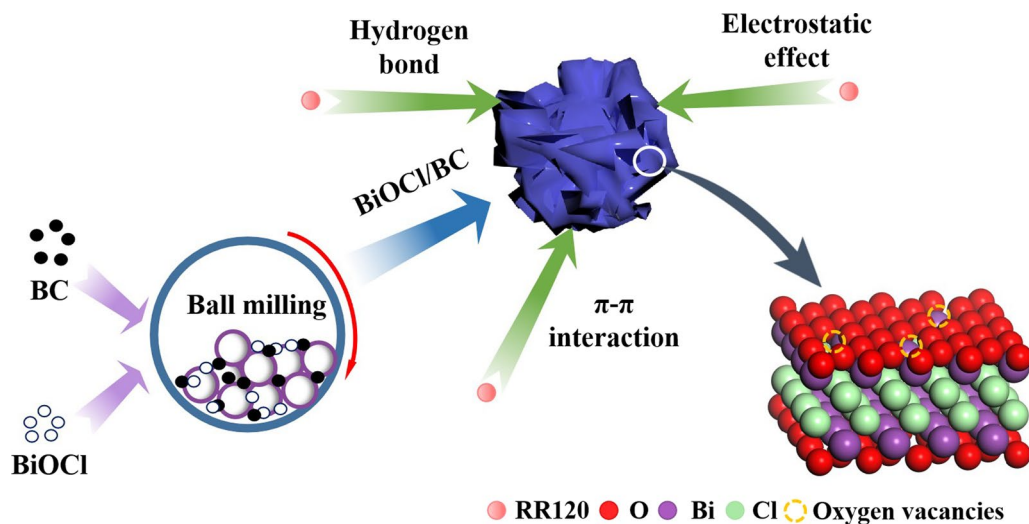
Yidan Luo<sup>1</sup> · Yonghu Wang<sup>1</sup> · Yaowei Zhu<sup>1</sup> · Mingshan Xue<sup>1</sup> · Aofeng Zheng<sup>1</sup> · Yu Han<sup>1</sup> · Zuozhu Yin<sup>1</sup> · Zhen Hong<sup>1</sup> · Chan Xie<sup>1</sup> · Xibao Li<sup>1</sup> · Sheng Lei<sup>2</sup> · Bin Gao<sup>3</sup>

Received: 18 September 2021 / Accepted: 2 March 2022  
© The Author(s) 2022

## Abstract

Fabricating surface oxygen vacancies is considered to be an efficient method to improve the adsorption performance of sorbents. In this work, a bismuth oxychloride/biochar (BiOCl/BC) nanocomposite with abundant oxygen vacancies was successfully prepared by a facile ball milling method. BiOCl/BC nanocomposite was found to have excellent adsorption performance for removing reactive red-120 (RR120) from aqueous solution. The effects of key adsorption parameters, such as RR120 dye concentration, solution pH (2–10), and contact time were studied by batch adsorption test. The adsorption data were well described by the Langmuir and Freundlich isotherms and pseudo-second-order kinetic models. The 50%-BiOCl/BC (50 wt% of BiOCl in composite) exhibited the best adsorptive performance (60%), much better than the pristine BM-BC (20%). The high adsorption capacity of 50%-BiOCl/BC (Langmuir maximum capacity of 116.382 mg g<sup>-1</sup>) can be attributed to the electrostatic effect,  $\pi$ - $\pi$  interactions, and hydrogen bond. This work provided a facile method to prepare semiconductor assisted biochar-based adsorbents, which would also contribute to the advance of environmental remediation.

## Graphical abstract



✉ Mingshan Xue  
xuems04@mailsucas.ac.cn

Extended author information available on the last page of the article

## Highlights

- BiOCl/biochar nanocomposites with rich oxygen vacancies were firstly synthesized by the ball milling method.
- Abundant oxygen vacancies on BiOCl/biochar nanocomposites improved its adsorption for reactive red-120.
- There were strong interactions between BiOCl and biochar after ball milling.

**Keywords** Bismuth oxychloride · Biochar · Reactive red-120 · Aqueous media · Oxygen vacancies · Adsorption mechanisms

## 1 Introduction

Due to the extensive demand and utilization of organic dyes in textile, cosmetics, papermaking, and other industries, there are high concentrations of toxic organic dyes in wastewater, which have serious impacts on the environment and human health. As one of the common anionic dyes (Mu'azu et al. 2018), RR120 contains azo ( $-N=N-$ ) groups, resulting in low biodegradability, and therefore poses many risks to the ecosystem and human health (Irem et al. 2013; Rahman et al. 2013). The high concentration of RR120 leads to skin irritation, dermatitis, carcinogenicity, mutagenicity, and toxicity to aquatic life. Hence, how to remove organic dyes before they are discharged into the water environment is extremely important for water treatment.

Numerous approaches include adsorption (Yagub et al. 2014), nanofiltration (Gerçel 2016), ion exchange (Liu et al. 2007), electrochemical catalysis (Zhang et al. 2019), and Fenton degradation (Hou et al. 2016) have been widely used to remove organic pollutants in wastewater. Compared to other technologies, adsorption is considered as one of the most efficient methods for removing organic dyes because of its easy operation, low cost, and high efficiency (Jang et al. 2018). Recently, biochar (BC) based materials as cost-efficient adsorbents have attracted much attention (Laird 2008; Zhang et al. 2017). The surfaces of most of the original biochars are usually negatively charged, which is related to their rich oxygen-containing functional groups, thus showing highly efficient adsorption of cation pollutants (Wang et al. 2017). However, most biochars have limited adsorption capacity for anionic dyes such as RR120, partly due to the lack of positive active sites on their surface (Yang et al. 2019; Zheng et al. 2020). This has greatly hindered the use of biochar to remove RR120 from aqueous solutions. Thus, improving the anionic dye adsorption capacity of biochar has become an important direction to expand the environmental applications of biochar technology.

Recently, metal oxide/biochar composites have been increasingly applied in adsorption for various water pollutants (Li et al. 2018; Yao et al. 2011). Chemical modification by loading metal oxides on the surface of biochar

can enhance its surface properties by adding more sorption sites and adjusting its surface charges, thereby improving its adsorption capacity (Zheng et al. 2020). Ball milling has been applied to fabricate carbon/metal oxide composites due to its low cost, environmental friendliness, and high efficiency (Kumar et al. 2020). On the one hand, ball milling can grind biochar into powder, which can decrease particle size, increase specific surface areas, and introduce surface functional groups on biochar, thus enhancing its adsorption ability (Cai et al. 2018; Lyu et al. 2020). On the other hand, ball milling of metal oxide can introduce lattice defects (such as oxygen vacancies) on its surface (Aggelopoulos et al. 2017). The presence of oxygen vacancies can change the state of the adsorbed molecules (e.g. bond length, bond angle, coordination mode, or intermediate), thereby increasing the affinity to the molecules (Zhao et al. 2020). Thus, it is very meaningful to adjust the adsorption properties of materials with the fabrication of oxygen vacancies by ball milling.

In this work, a series of oxygen vacancy-rich BiOCl/biochar nanocomposites were prepared by solvent-free ball-milling of BiOCl particles and biochar. A series of adsorption experiments were conducted to evaluate the RR120 adsorption capacity of composite materials. The ball-milling parameters such as time, speed, and ratio of balls-to-BiOCl were investigated. The physicochemical properties of BiOCl/biochar nanocomposites were characterized. Moreover, the adsorption behaviors and mechanisms for RR120 on BiOCl/biochar nanocomposites were studied in particular. The presented investigation provided new ideas in the field of biochar-based adsorbents.

## 2 Experimental section

### 2.1 Catalyst preparation

The bamboo was cut into small pieces and washed with deionized water for further use. Fast pyrolysis of bamboo at 800 °C was conducted to produce biochar (Hien et al. 2020).

The obtained biochar was washed thoroughly with deionized water and dried at 60 °C overnight for further use.

For the preparation of BiOCl, Bi(NO<sub>3</sub>)<sub>3</sub>·5H<sub>2</sub>O (0.02 mol) and KCl (0.02 mol) were added into ethylene glycol (90 mL, AR 98%) with stirring to obtain a homogeneous solution. After magnetic stirring for 30 min, the mixture was transferred to a hydrothermal container (100 mL) and was heated in an oven at 160 °C for 12 h. After heating, the resulting precipitate was centrifuged and alternately washed three times each by ethanol and distilled water. The obtained sample was named as BiOCl.

The nanocomposites of BiOCl/BC were made by the facile ball milling method. The procedures of ball-milling were as follows: mixtures (4 g) of BiOCl and biochar with different mass percentages of BiOCl (1%, 10%, 30%, 50%, 60%, and 80%) were put in 250 mL ball milling jars and then 200 g balls were added into each jar. The ball milling was operated at a rotational speed of 400 rpm for 9 h and the rotation direction was altered every 1.5 h. A series of BiOCl/BC nanocomposites with different mass percentages of BiOCl (1%, 10%, 30%, 50%, 60%, and 80%) were obtained and marked as 1%-BiOCl/BC, 10%-BiOCl/BC, 30%-BiOCl/BC, 50%-BiOCl/BC, 60%-BiOCl/BC, and 80%-BiOCl/BC. The diameter of 50%-BiOCl/BC nanoparticles is about 0.2–1 μm. The BM-BiOCl and BM-BC were also prepared with the same procedures in the absence of biochar or BiOCl, respectively.

## 2.2 Catalyst characterization

Powder X-ray diffraction measurements were characterized by X-ray diffractometer (Bruker D8 Advance-A25, Germany) in a scanning range of 5°–80° (2 theta) with Cu Kα (λ = 0.15418 nm) radiation. Fourier-transform infrared spectroscopy (FT-IR) spectra of samples were measured from 400 to 4000 cm<sup>-1</sup> on an FT-IR spectrometer (Bruker VERTEX 70, Germany). The surface microstructure was obtained using a Nova Nano SEM-450 (FEI, USA) field emission scanning electron microscopy (FE-SEM). Transmission electron microscopy (TEM, JEOL 2100F, Japan) was employed to observe the internal structural morphology. X-ray photoelectron spectroscopy (XPS) measurements were acquired on an X-ray photoelectron spectrometer (Thermo Scientific ESCALAB 250, USA) with an Al Kα radiator. All the binding energy values were calibrated by the C 1s peak at 284.8 eV. Brunauer–Emmett–Teller (BET) surface area and pore size measurements were tested by nitrogen adsorption via an adsorption–desorption instrument (Quantachrome Autosorb-iQ, USA). Electron paramagnetic resonance (EPR) spectra were recorded at room temperature using a Bruker A300 (Germany, Bruker). Zeta potential data were measured with a 90Plus PALS high sensitivity zeta potential and particle size analyzer (Brookhaven, USA).

## 2.3 Batch adsorption experiment

The optimum ball milling parameters were investigated by batch adsorption experiments. The preparation details of BM-BiOCl under different ball-milling conditions can be seen in the Additional file 1 (S1). For each experiment, adsorbent (dosage of 0.4 g L<sup>-1</sup>) was added into 15 mL of RR120 solution (10 mg L<sup>-1</sup>) under mechanical shaking at 25 °C for 24 h. After shaking, the suspension was filtered with 0.22 μm filter membrane (MCE, Troody). RR120 concentration was measured at 533 nm by UV mini-1285 (Shimadzu, Japan). To make the experimental results more accurate, all experiments were repeated three times.

The sample with the highest RR120 removal rate (50%-BiOCl/BC) was selected to further investigate the adsorption behavior of RR120 on BiOCl/BC nanocomposites. The adsorption capacity ( $q_e$ , mg g<sup>-1</sup>) and removal efficiency (R%) can be calculated by Eqs. (1) and (2):

$$q_e = \frac{(C_0 - C_e)V}{m} \quad (1)$$

$$R = \frac{C_0 - C_e}{C_0} \times 100\% \quad (2)$$

where  $C_0$  and  $C_e$  are the initial and ultimate detected concentrations (mol L<sup>-1</sup>) of the RR120 solution, respectively, and  $V$  (L) and  $m$  (g) represent the volume of RR120 solution and the mass of adsorbent.

## 3 Results and discussion

### 3.1 Characterization of BiOCl/BC nanocomposites

The crystal structures of the as-prepared samples were studied by XRD. As shown in Fig. 1a, the XRD pattern of the BM-BC showed a low-intensity diffraction peak around 26.6°, corresponding to hexagonal carbon (JCPDS NO. 26-1076). The XRD pattern of BM-BiOCl exhibited the characteristic diffraction peaks at 11.9°, 26.0°, 32.5°, 33.6°, 40.9°, 46.8°, and 58.6°, corresponding to (001), (101), (110), (102), (112), (200), and (212) crystal planes of tetragonal phase of BiOCl (JCPDS No. 85-0861), respectively. The diffraction peaks of BiOCl also existed in the XRD patterns of BiOCl/BC nanocomposites, indicating that the formation of the nanocomposites did not significantly change the crystallinity of BiOCl. The peak of biochar almost disappeared in the composites, due to the good dispersion of biochar in composites.

Figure 1b shows the FTIR spectra of the as-prepared BM-BiOCl, 50%-BiOCl/BC, and BM-BC to better understand the chemical structure of the prepared BiOCl/BC

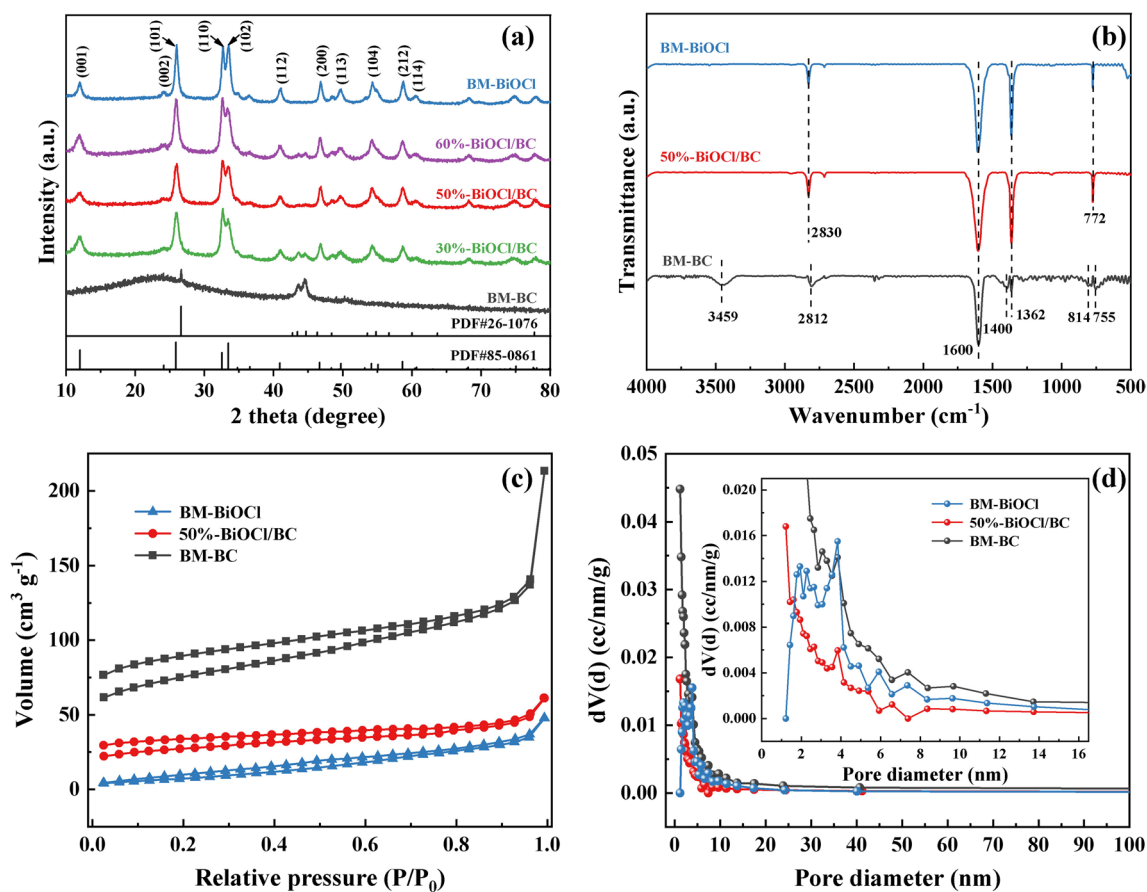


**Fig. 1** XRD patterns (a) of BM-BiOCl, 60%-BiOCl, 50%-BiOCl, 30%-BiOCl and BM-BC; FTIR spectra (b), N<sub>2</sub> adsorption–desorption isotherms (c), and pore volume distribution curves (d) of BM-BiOCl, 50%-BiOCl/BC, and BM-BC

nanocomposites. The observed peaks in BM-BC were allocated as: at 3459 cm<sup>-1</sup> (O–H vibrational stretching and N–H stretching vibration) (He et al. 2019); 2812 cm<sup>-1</sup> (asymmetric CH<sub>2</sub> stretching) (Amjed et al. 2020); 1600 cm<sup>-1</sup> (O–H bending) (Micheal et al. 2019); 1400, 1362 cm<sup>-1</sup> (O–H stretching) (Tang et al. 2021); 814, 755 cm<sup>-1</sup> (aromatic C–H bending) (Mingke et al. 2019). The absorption peaks at 2830 (Boukaoud et al. 2021), 1600, 1362, and 772 cm<sup>-1</sup> (Wang et al. 2015) in BM-BiOCl can be attributed to the O–H stretching, O–H bending, O–H stretching, and the asymmetrical stretching vibration of the Bi–O bond, respectively. The similar FTIR spectra of BM-BiOCl and 50%-BiOCl/BC indicate that the structures of BiOCl are not changed after the introduction of BC.

The nitrogen adsorption–desorption isotherms (Fig. 1c) show that the adsorption isotherm of BM-BiOCl was type IV isotherm with H3 hysteresis loop according to the IUPAC classification (Kruk and Jaroniec 2001; Sing 1985), implying that it comprised of aggregates of platelike particles forming slitlike pores. The isotherms of BiOCl/BC nanocomposites and BM-BC did not enclose, which may attribute to the existence of a large amount of very narrow slit pores

**Table 1** Specific surface areas and pore characteristics of the BM-BiOCl, 50%-BiOCl/BC, and BM-BC samples

Samples	Surface area (m <sup>2</sup> g <sup>-1</sup> )	Pore size (nm)	Pore volume (cm <sup>3</sup> g <sup>-1</sup> )
BM-BiOCl	43.96	2.847	0.0800
50%-BiOCl/BC	62.15	2.642	0.0761
BM-BC	163.7	1.771	0.2765

or bottle-shaped pores in the biochar (Wang et al. 2018). Pore diameter analysis (Fig. 1d) showed that BM-BiOCl had many pores ranging from 2 to 4 nm, while BM-BC and 50%-BiOCl/BC exhibited many micropores which is due to the pore structure of biochar. The BET surface area, pore size, and pore volume of BM-BC, BM-BiOCl, and 50%-BiOCl/BC were estimated by N<sub>2</sub> adsorption–desorption isotherms. As shown in Table 1, the specific surface area of 50%-BiOCl/BC (62.15 m<sup>2</sup> g<sup>-1</sup>) was lower than that of BM-BC (163.7 m<sup>2</sup> g<sup>-1</sup>) but higher than that of BM-BiOCl (43.96 m<sup>2</sup> g<sup>-1</sup>), indicating that the introduction of BC increased the specific surface area of the BiOCl/BC nanocomposites



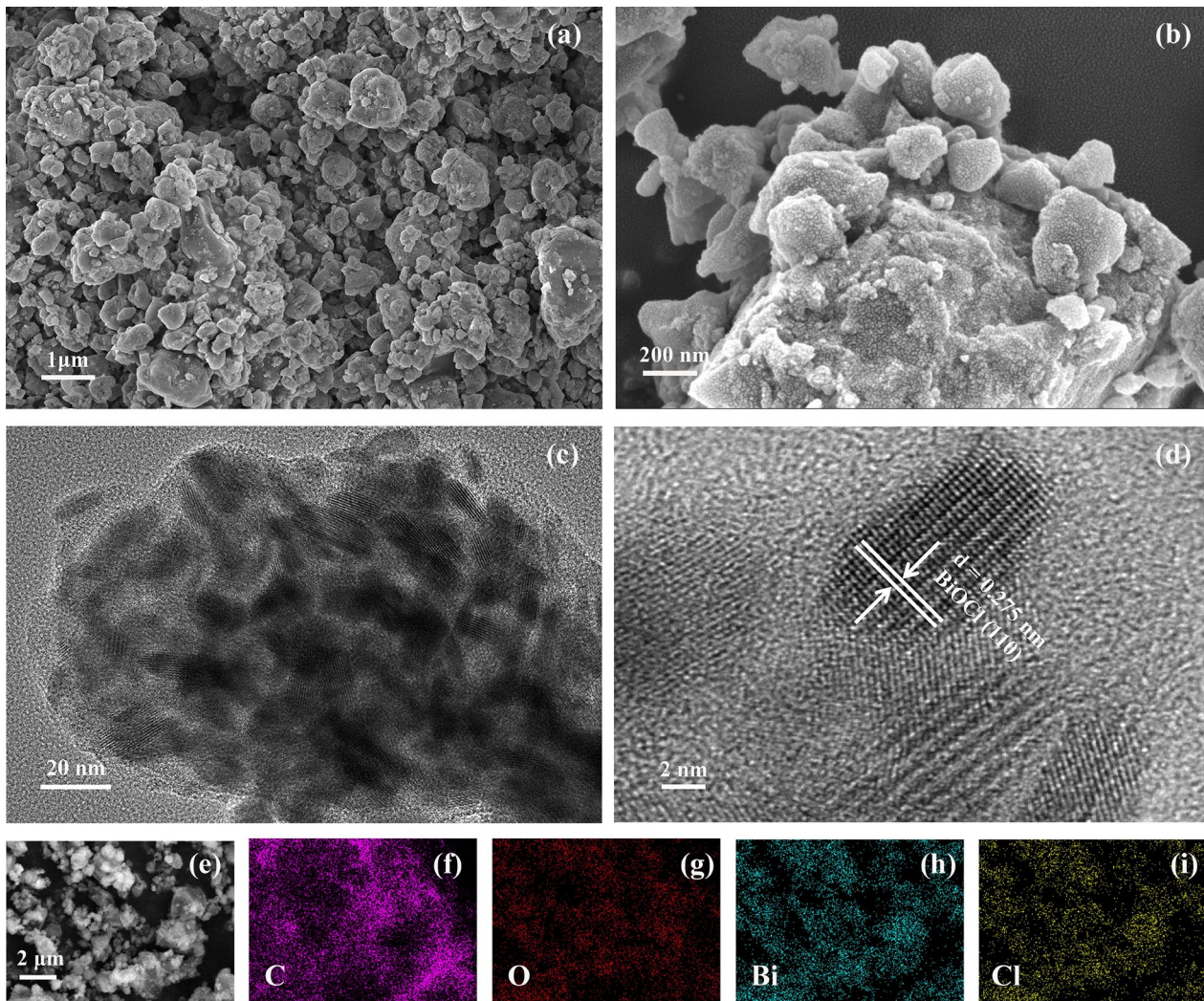


**Fig. 2** SEM images (a, b) of 50% BiOCl/BC; TEM image (c) and HRTEM image (d) of 50%-BiOCl/BC; the EDS mapping images (f–i) of 50%-BiOCl/BC image (e)

compared to BM-BiOCl, which may enhance the adsorption capacity of RR120.

The SEM images (Fig. 2a, b) of 50%-BiOCl/BC showed that the diameters of nanocomposite nanoparticles were about 0.2–1  $\mu\text{m}$ . EDS analysis (Fig. 2e–i) proved that the C, O, Bi, and Cl elements were uniformly distributed in 50%-BiOCl/BC. To further examine the microstructure of 50%-BiOCl/BC, TEM and HRTEM images were obtained and shown in Fig. 2c and d. Small BiOCl nanoparticles with diameters around 10–25 nm were distributed in biochar. Clear lattice fringes of 0.275 nm can be observed corresponding to the (110) crystal facets of BiOCl. The TEM and HRTEM analysis further proved that BiOCl nanoparticles were evenly distributed on BC.

The XPS measurement was performed to reveal the surface composition and chemical state of as-prepared samples. Figure 3a shows that the 50%-BiOCl/BC was composed of

the elements of Bi, O, Cl, and C. The O 1s XPS spectrum (Fig. 3b) of BM-BiOCl can be resolved into three peaks. The binding energies at 529.9 eV, 530.8 eV, and 531.9 eV can be assigned to Bi–O bond, oxygen vacancies, and adsorbed oxygen such as hydroxyl groups or  $\text{O}_2$  molecules, respectively (Lu et al. 2019; Yang et al. 2020). In the O 1s of BM-BC, the binding energies at 532.3 eV and 533.8 eV can be assigned to adsorbed oxygen and C–O bond (Quan et al. 2020). The O 1s spectrum of 50%-BiOCl/BC can be convoluted into four peaks: Bi–O bond (530.3 eV), oxygen vacancies (531.1 eV), adsorbed oxygen (532.1 eV), and C–O bond (532.8 eV). The peaks of O 1s of 50%-BiOCl/BC shifted to the higher binding energy compared to BM-BiOCl and to lower binding energy compared to BM-BC, indicating the interactions between BiOCl and BC in the composite. Figure 3c shows two peaks in Cl 2p of BM-BiOCl spectrum at 198.0 eV and 199.6 eV can be assigned to Cl 2p<sub>3/2</sub> and

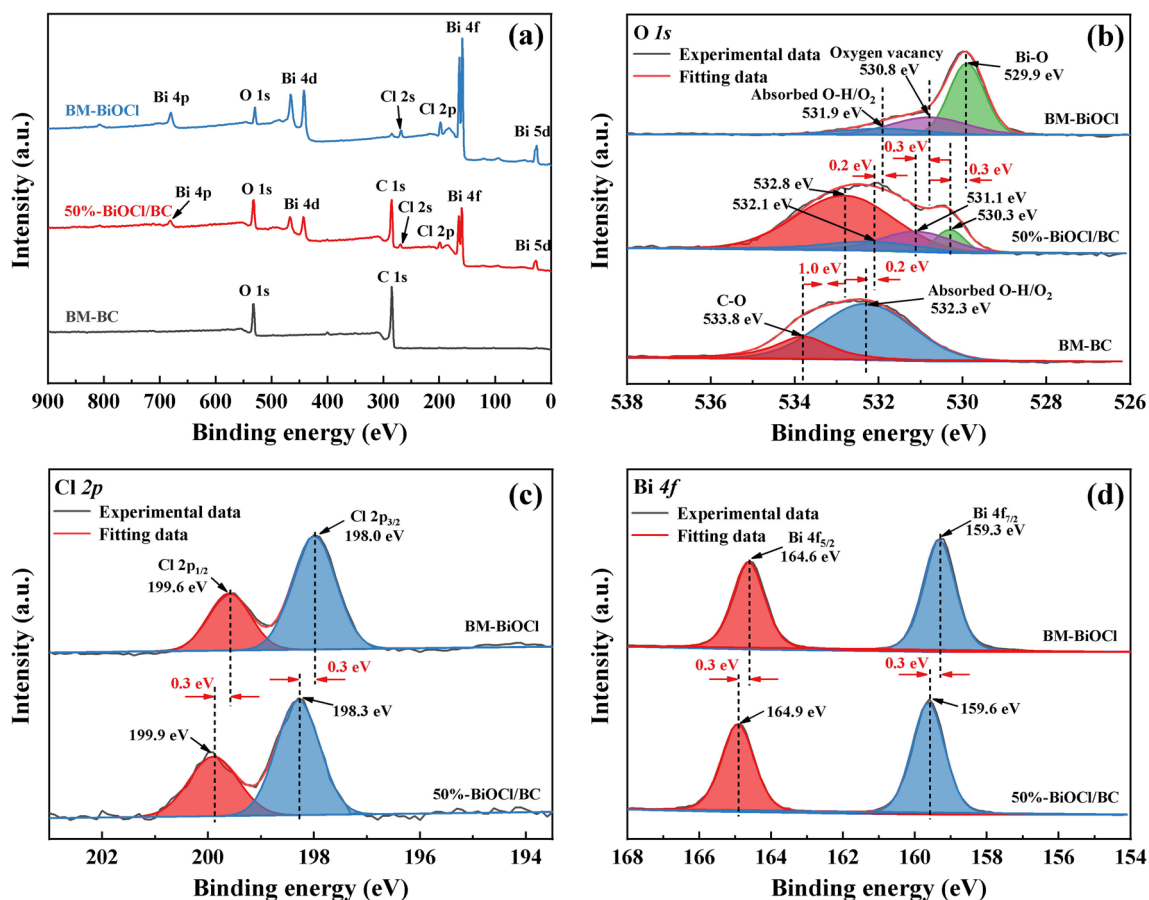


**Fig. 3** Survey spectra (a) and O 1s spectra (b) of BM-BiOCl, 50%-BiOCl/BC, and BM-BC; Cl 2p (c) and Bi 4f (d) spectra for BM-BiOCl and 50%-BiOCl/BC

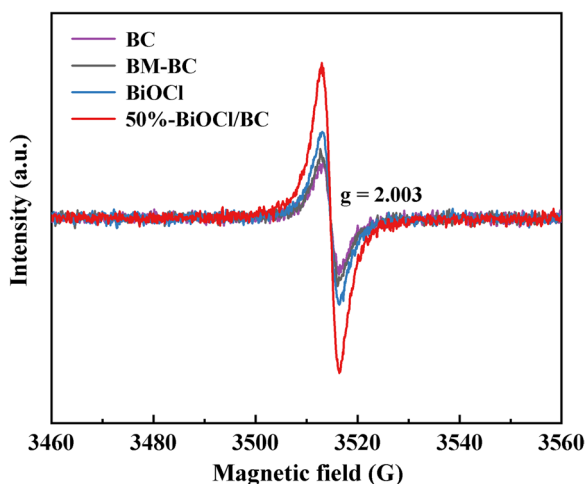


**Fig. 4** EPR spectra of BC, BM-BC, BiOCl, and 50%-BiOCl/BC

Cl  $2p_{1/2}$ , respectively, which were characteristic peaks of Cl atoms in the BM-BiOCl (Cai et al. 2018). Two peaks in Bi 4f spectrum of BM-BiOCl at 159.3 eV and 164.6 eV (Fig. 3d) belong to Bi  $4f_{7/2}$  and Bi  $4f_{5/2}$ , respectively (Wu et al. 2017). Compared with BM-BiOCl, the characteristic peaks of Cl and Bi in 50%-BiOCl/BC moved to higher binding energy, indicating the electron density on the surface of Bi and Cl decreased in the composites, which is also due to the strong interactions between BiOCl and biochar in composites.

In addition, electron paramagnetic resonance (EPR) measurements were carried out to detect surface oxygen vacancies, because the presence of oxygen vacancy leads to obvious electron paramagnetic resonance (EPR) signals when  $g = 2.003$  (Zhang et al. 2020). As shown in Fig. 4, the 50%-BiOCl/BC showed a strong characteristic EPR signal, indicating the existence of large amounts of oxygen vacancies. The concentration of oxygen vacancies in 50%-BiOCl/

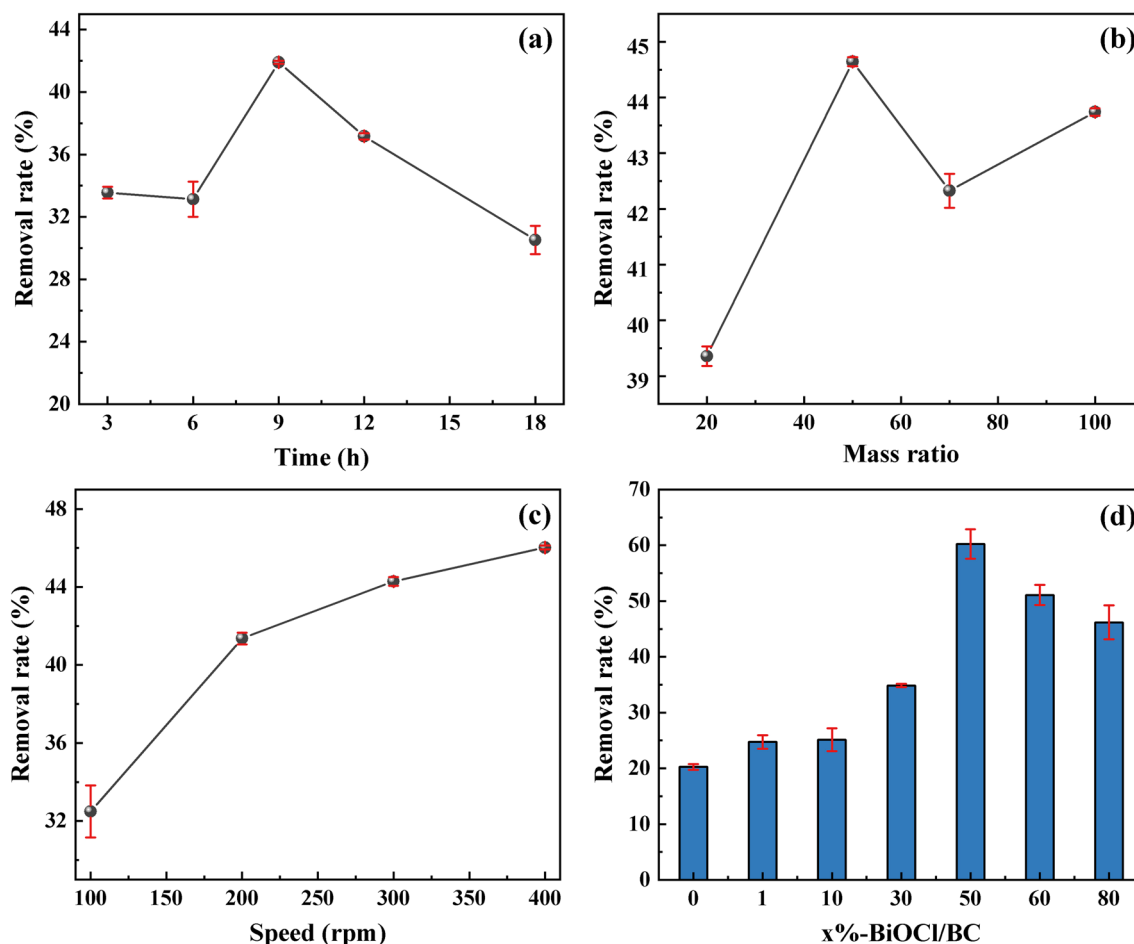


**Fig. 5** RR120 sorption capacity on BiOCl with different milling time (a), mass percentage (b), and speed (c); effect of BiOCl content (d) on RR120 adsorption on BiOCl/BC nanocomposites

BC was higher than in BiOCl, BC (Liu et al. 2017; Sun et al. 2018), and BM-BC samples, which may provide more active sites for adsorption.

### 3.2 Comparison of the best ball milling parameters and the adsorption capacity of different ratios in composites

Because BiOCl was the modification component in nanocomposites, ball milling parameters were optimized based on the RR120 adsorption capacities of BiOCl. BM-BiOCl powders with different ball-milling times, ball-milling speeds, and mass ratio of ball to BiOCl were prepared, and then subjected to batch adsorption experiments to obtain the best ball milling parameters. The RR120 adsorption capacity of BM-BiOCl samples under different ball milling conditions are shown in Fig. 5a–c. The mass ratio of ball to BiOCl had little effect on the adsorption capacity of RR120 on BiOCl, while the ball milling speed and ball milling time showed greater influences.

The optimum milling parameters were as follows: milling time was 9 h, the mass ratio of balls to BiOCl was 50:1, and milling speed was 400 rpm. Subsequently, ball milling samples were obtained under the optimum milling parameters.

Figure 5d shows the effect of different mass percentages of BiOCl to BC on the adsorption capacity of RR120. Compared with BM-BC, all the BiOCl/BC nanocomposites showed higher removal rate of RR120, which reflected that the adsorption capacity of biochar to RR120 was significantly enhanced after ball milling with BiOCl. The removal rate of RR120 by BiOCl/BC nanocomposites with the increase of BiOCl content, and the removal rate reached the highest at 50%-BiOCl/BC. However, further increase of the content of BiOCl in BiOCl/BC nanocomposites reduced the RR120 adsorption capacity of nanocomposites. This might be due to the aggregations of BiOCl nanoparticles in the composites when BiOCl contents were further increased.



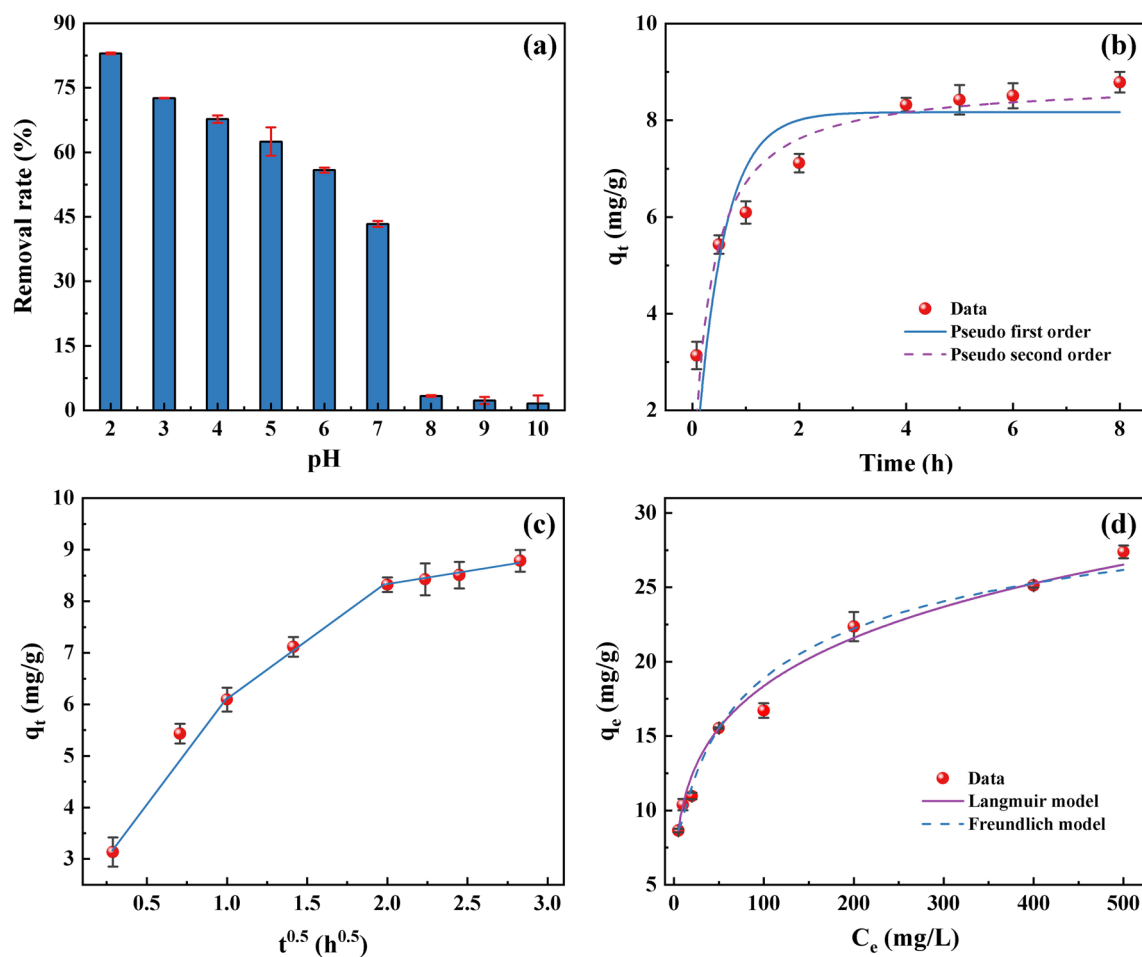


**Fig. 6** The effect of solution pH on the adsorption of RR120 (a); kinetics of RR120 adsorption on 50%-BiOCl/BC (vs time) (b); kinetics of RR120 adsorption on 50%-BiOCl/BC (vs square root of time)

(c); isotherms of RR120 on 50%-BiOCl/BC (d). The lines are simulations of various models

**Table 2** Best-fit parameters of the kinetics and isotherm models for RR120 adsorption on 50%-BiOCl/BC

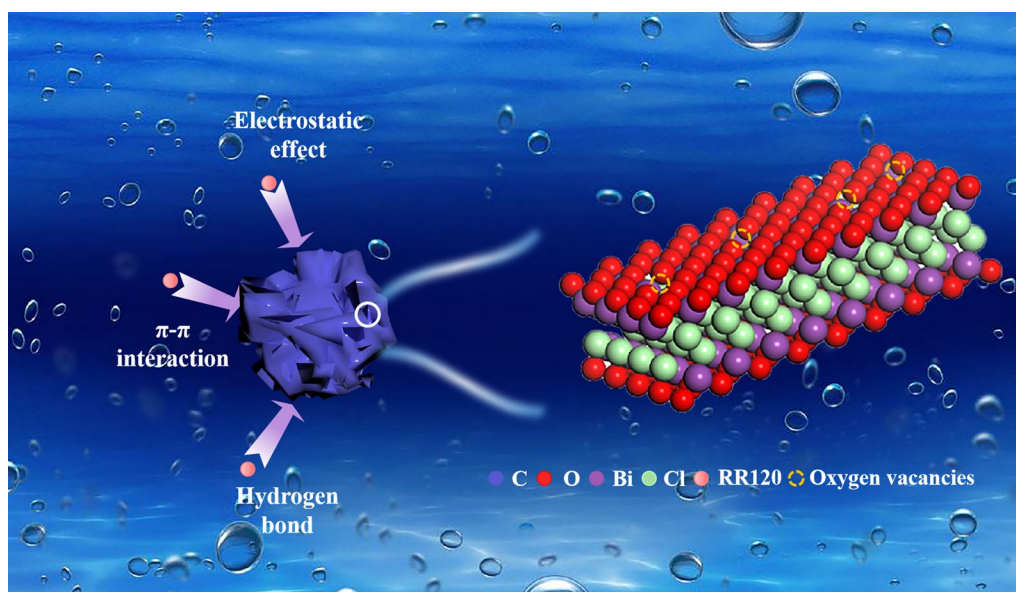
Model	Parameter 1	Parameter 2	R <sup>2</sup>
Pseudo-first-order	$K_1 = 1.956 \text{ h}^{-1}$	$q_e = 8.169 \text{ mg g}^{-1}$	0.794
Pseudo-second-order	$K_2 = 0.313 \text{ g mg}^{-1} \text{ h}^{-1}$	$q_e = 8.809 \text{ mg g}^{-1}$	0.920
Langmuir	$K_L = 0.051 \text{ mg}^{-1}$	$q_m = 116.382 \text{ mg g}^{-1}$	0.999
Freundlich	$K_F = 36.493 \text{ mg}^{(1-n)} \text{ L}^n \text{ g}^{-1}$	$n_F = 2.380$	0.998

### 3.3 Adsorption behaviors

The parameter of pH is a key factor that affects the dye adsorption process, because it controls the degree of ionization of adsorbed molecules and the surface charge of the adsorbent. Figure 6a describes the effect of initial solution pH on the adsorption of RR120 on 50%-BiOCl/BC. It was observed that with the rising of pH from 2 to 10, the removal rate gradually decreased from 62.5 to 1.6%. The highest adsorption capacity of RR120 dye was observed at solution pH 2. The  $\text{pH}_{\text{pzc}}$  (point of zero charge) of 50%-BiOCl/BC

was tested to be 2.1 (Additional file 1: Fig. S1) (Azalok et al. 2021). Errais et al. measured aqueous solution of RR120 dye by potentiometric titration, the results showed that RR120 dye still had anionic morphology at acidic pH ( $\text{pH} < 4$ ) (Errais et al. 2012). Therefore, when the solution pH was below 2.1, the surface of 50%-BiOCl/BC can be converted to positively charged, thus promoting the uptake of negatively charged species (RR120) via electrostatic attraction (Jawad et al. 2020a, b). With the pH increase, the electrostatic attraction gradually weakened, while hydrogen bond and  $\pi$ - $\pi$  interactions were the main functional mechanisms.





**Scheme 1** Schematic diagram of adsorption mechanism for RR120 on 50%-BiOCl/BC

In summary, 50%-BiOCl/BC exhibited better adsorption ability at lower pH for RR120 dye.

The efficiency of adsorbents was characterized by adsorption kinetics. Figure 6b shows the experimental data and model fitting of adsorption kinetics. It can be observed that the adsorption kinetic rate of RR120 on 50%-BiOCl/BC increased sharply in the first 1 h, then slowed down with time, reaching adsorption equilibrium within 4 h. Table 2 summarizes the two different adsorption kinetics models' best model parameters and corresponding correlation coefficients. Compared with the pseudo-first-order model ( $R^2 = 0.794$ ), the pseudo-second-order model ( $R^2 = 0.920$ ) fitted better. This suggests that the adsorption of RR120 dye on the 50%-BiOCl/BC was more likely to be controlled by the chemical adsorption process (Zubair et al. 2020). The curve of adsorption kinetics versus  $t^{0.5}$  showed three straight lines (Fig. 6c), indicating that the adsorption kinetics of RR120 on nanocomposites might be divided into three steps (Lyu et al. 2018). The initial rapid adsorption might be due to the electrostatic attraction between the positively charged 50%-BiOCl/BC surface and the negatively charged RR120, while the later slow adsorption suggested that intra-particle diffusion may be involved (Lalley et al. 2016). Finally, the adsorption of RR120 by the composites hardly changed.

Figure 6d shows the adsorption isotherms of RR120 on 50%-BiOCl/BC. It can be seen that 50%-BiOCl/BC showed high adsorption ability of RR120 in a wide range of equilibrium concentrations, reflecting that the 50%-BiOCl/BC had a large adsorption capacity for RR120. The experimental data were simulated with Freundlich and Langmuir models,

and the best model parameters were summarized in Table 2. Freundlich ( $R^2 = 0.998$ ) model and Langmuir ( $R^2 = 0.999$ ) both described the isotherm data well with the  $R^2$  values close to each other. The Langmuir model fitted slightly better than the Freundlich model, indicating that the single-layer adsorption behavior was dominant (Fan et al. 2019; Jang et al. 2018). The adsorption kinetics and isotherms results showed that 50%-BiOCl/BC could be used as an effective adsorbent for RR120 dye.

To evaluate the stability of 50%-BiOCl/BC in RR120 solution, the XRD patterns before and after the adsorption of RR120 by 50%-BiOCl/BC were measured (Additional file 1: Fig. S2). It can be seen that the XRD patterns of the sample before and after adsorption did not change significantly, which can prove that it was stable in aqueous solution. The corresponding pictures of 50%-BiOCl/BC sample before and after adsorption were barely changed (Inserts in Additional file 1: Fig. S2), which further proved the stability of the adsorbent.

### 3.4 Adsorption mechanisms

Based on the above discussion of BET surface area, oxygen vacancies, pH effects, adsorption kinetics, and adsorption isotherms, the possible adsorption mechanisms of 50%-BiOCl/BC were analyzed and illustrated in Scheme 1. High specific surface area and porous structures contributed to the adsorption performance of the prepared BiOCl/BC composites. Abundant oxygen vacancies on the surface of the 50%-BiOCl/BC provided a large number of adsorption sites and also improved its adsorption for RR120 dye (Zhao et al.

2020). When  $\text{pH} < \text{pH}_{\text{pzc}}$  ( $\text{pH}_{\text{pzc}} 2.1$ ), electrostatic attractions existed between negatively charged sulfonate ( $-\text{SO}_3^-$ ) acid groups of RR120 and the positively charged surface of 50%-BiOCl/BC. Hydroxyl bond can occur between  $-\text{OH}$  on the surface of 50%-BiOCl/BC and aromatic ring or O and N atoms in RR120 dye (Jawad et al. 2019, 2020c). The benzene rings of RR120 molecules could interact with the benzene ring of biochar in 50%-BiOCl/BC through  $\pi-\pi$  interactions (Gai et al. 2020). Thus, it can be inferred that high specific surface area, abundant oxygen vacancies, electrostatic effect, hydrogen bond, and  $\pi-\pi$  interaction determined the adsorption capacity of 50%-BiOCl/BC.

## 4 Conclusion

In this work, the 50%-BiOCl/BC showed high adsorption capacity for RR120 dye (62%), which was much higher than that of BM-BC (20%). Through batch adsorption experiments, the effects of key adsorption parameters such as RR120 concentration, solution pH, and contact time were studied. Langmuir model, Freundlich model, and pseudo-second-order kinetic model described the adsorption process well. The electrostatic effect,  $\pi-\pi$  interaction, and hydrogen bond might be the adsorption mechanism on the heterogeneous surface, and intra-particle diffusion will be the main limitation of RR120 adsorption on 50%-BiOCl/BC. As a result, the ball-milled BiOCl/BC nanocomposites enhanced physicochemical properties and efficient removal ability for RR120 dye from wastewater.

**Supplementary Information** The online version contains supplementary material available at <https://doi.org/10.1007/s42773-022-00147-0>.

**Acknowledgements** Not applicable.

**Authors' contributions** MX and BG proposed the research. YL and YW designed and conducted the experiments and analyzed the experimental results. ZH and ZY organized data, including research literature and drawing. CX, XL, and SL performed the physicochemical and photochemical characterization of as-synthesized materials. YZ, AZ, and YH synthesized the target biochar-based nanocomposite. All authors discussed the results and commented on the manuscript.

**Funding** This work was supported by the National Natural Science Foundation of China (11864024), Jiangxi Provincial Natural Science Foundation (20202BABL214025, 20202BABL214010, 20212BAB214034).

**Availability of data and materials** All data are available upon request.

## Declarations

**Conflict of interest** The authors declare that they have no known competing financial interests or personal relationships that could have appeared to influence the work reported in this paper.

**Ethics approval and consent to participate** Not applicable.

**Consent for publication** Not applicable.

**Open Access** This article is licensed under a Creative Commons Attribution 4.0 International License, which permits use, sharing, adaptation, distribution and reproduction in any medium or format, as long as you give appropriate credit to the original author(s) and the source, provide a link to the Creative Commons licence, and indicate if changes were made. The images or other third party material in this article are included in the article's Creative Commons licence, unless indicated otherwise in a credit line to the material. If material is not included in the article's Creative Commons licence and your intended use is not permitted by statutory regulation or exceeds the permitted use, you will need to obtain permission directly from the copyright holder. To view a copy of this licence, visit <http://creativecommons.org/licenses/by/4.0/>.

## References

- Aggelopoulos CA, Dimitropoulos M, Govatsi A, Sygellou L, Tsakiroglou CD, Yannopoulos SN (2017) Influence of the surface-to-bulk defects ratio of ZnO and TiO<sub>2</sub> on their UV-mediated photocatalytic activity. *Appl Catal B* 205:292–301. <https://doi.org/10.1016/j.apcatb.2016.12.023>
- Amjed N, Bhatti IA, Zia KM, Iqbal J, Jamil Y (2020) Synthesis and characterization of stable and biological active chitin-based polyurethane elastomers. *Int J Biol Macromol* 154:1149–1157. <https://doi.org/10.1016/j.ijbiomac.2019.11.097>
- Azalok KA, Oladipo AA, Gazi M (2021) Hybrid MnFe-LDO-biochar nanopowders for degradation of metronidazole via UV-light-driven photocatalysis: characterization and mechanism studies. *Chemosphere* 268:128844. <https://doi.org/10.1016/j.chemosphere.2020.128844>
- Boukaoud A, Chiba Y, Fatimi K, Yahimi N, Meguellati FZ, Bouguetaya S (2021) IR spectroscopy and computational study of structural, vibrational and electronic properties of hydrindantin dihydrate. In: *Advances in green energies and materials technology*. Springer, Singapore, pp 17–23. [https://doi.org/10.1007/978-981-16-0378-5\\_3](https://doi.org/10.1007/978-981-16-0378-5_3)
- Cai Y, Li D, Sun J, Chen M, Li Y, Zou Z, Zhang H, Xu H, Xia D (2018) Synthesis of BiOCl nanosheets with oxygen vacancies for the improved photocatalytic properties. *Appl Surf Sci* 439:697–704. <https://doi.org/10.1016/j.apsusc.2018.01.089>
- Errais E, Duplay J, Elhabiri M, Khodja M, Ocampo R, Baltenweck-Guyot R, Darragi F (2012) Anionic RR120 dye adsorption onto raw clay: surface properties and adsorption mechanism. *Colloids Surf A* 403:69–78. <https://doi.org/10.1016/j.colsurfa.2012.03.057>
- Fan YA, Sz A, Ys B, Dcwt B, Kc C, Yong S (2019) Assembling biochar with various layered double hydroxides for enhancement of phosphorus recovery—ScienceDirect. *J Hazard Mater* 365:665–673. <https://doi.org/10.1016/j.jhazmat.2018.11.047>
- Gai S, Zhang J, Fan R, Xing K, Chen W, Zhu K, Zheng X, Wang P, Fang X, Yang Y (2020) Highly stable zinc-based metal-organic frameworks and corresponding flexible composites for removal and detection of antibiotics in water. *ACS Appl Mater Interfaces* 12:8650–8662. <https://doi.org/10.1021/acsami.9b19583>
- Gerçel Ö (2016) Removal of textile dye from aqueous solution by electrochemical method. *Sep Sci Technol* 51:711–717. <https://doi.org/10.1080/01496395.2015.1088870>
- He X, Yang DP, Zhang X, Liu M, Kang Z, Lin C, Jia N, Luque R (2019) Waste eggshell membrane-templated CuO–ZnO nanocomposites

- with enhanced adsorption, catalysis and antibacterial properties for water purification. *Chem Eng J* 369:621–633. <https://doi.org/10.1016/j.cej.2019.03.047>
- Hien TTT, Tsubota T, Taniguchi T, Shinogi Y (2020) Enhancing soil water holding capacity and provision of a potassium source via optimization of the pyrolysis of bamboo biochar. *Biochar* 3:51–61. <https://doi.org/10.1007/s42773-020-00071-1>
- Hou X, Huang X, Ai Z, Zhao J, Zhang L (2016) Ascorbic acid/Fe@Fe<sub>2</sub>O<sub>3</sub>: a highly efficient combined Fenton reagent to remove organic contaminants. *J Hazard Mater* 310:170–178. <https://doi.org/10.1016/j.jhazmat.2016.01.020>
- Irem, S, Khan Q M, Islam E, Hashmat A J, ul Haq M A, Afzal M, Mustafa T (2013) Enhanced removal of reactive navy blue dye using powdered orange waste. *Ecol Eng* 58:399–405. <https://doi.org/10.1016/j.ecoleng.2013.07.005>
- Jang HM, Yoo S, Choi Y-K, Park S, Kan E (2018) Adsorption isotherm, kinetic modeling and mechanism of tetracycline on *Pinus taeda*-derived activated biochar. *Bioresour Technol* 259:24–31. <https://doi.org/10.1016/j.biortech.2018.03.013>
- Jawad AH, Mubarak NSA, Sabar S (2019) Adsorption and mechanism study for reactive red 120 dye removal by cross-linked chitosan-epichlorohydrin biobeads. *Desalin Water Treat* 164:378–387. <https://doi.org/10.5004/dwt.2019.24438>
- Jawad AH, Abdulhameed AS, Reghioua A, Yaseen ZM (2020a) Zwitterion composite chitosan-epichlorohydrin/zeolite for adsorption of methylene blue and reactive red 120 dyes. *Int J Biol Macromol* 163:756–765. <https://doi.org/10.1016/j.ijbiomac.2020.07.014>
- Jawad AH, Mubarak NSA, Abdulhameed AS (2020b) Hybrid crosslinked chitosan-epichlorohydrin/TiO<sub>2</sub> nanocomposite for reactive red 120 dye adsorption: kinetic, isotherm, thermodynamic, and mechanism study. *J Polym Environ* 28:624–637. <https://doi.org/10.1007/s10924-019-01631-8>
- Jawad AH, Mubarak NSA, Abdulhameed AS (2020c) Tunable Schiff's base-cross-linked chitosan composite for the removal of reactive red 120 dye: adsorption and mechanism study. *Int J Biol Macromol* 142:732–741. <https://doi.org/10.1016/j.ijbiomac.2019.10.014>
- Kruk M, Jaroniec M (2001) Gas adsorption characterization of ordered organic–inorganic nanocomposite materials. *Chem Mater* 13:3169–3183. <https://doi.org/10.1021/cm0101069>
- Kumar M, Xiong X, Wan Z, Sun Y, Tsang DC, Gupta J, Gao B, Cao X, Tang J, Ok YS (2020) Ball milling as a mechanochemical technology for fabrication of novel biochar nanomaterials. *Bioresour Technol* 312:123613. <https://doi.org/10.1016/j.biortech.2020.123613>
- Laird DA (2008) The charcoal vision: a win–win–win scenario for simultaneously producing bioenergy, permanently sequestering carbon, while improving soil and water quality. *Agron J* 100:178–181. <https://doi.org/10.2134/agronj2007.0161>
- Lalley J, Han C, Li X, Dionysiou D, Nadagouda MN (2016) Phosphate adsorption using modified iron oxide-based sorbents in lake water: kinetics, equilibrium, and column tests. *Chem Eng J* 284:1386–1396. <https://doi.org/10.1016/j.cej.2015.08.114>
- Li R, Wang JJ, Gaston LA, Zhou B, Li M, Xiao R, Wang Q, Zhang Z, Huang H, Liang W (2018) An overview of carbothermal synthesis of metal–biochar composites for the removal of oxyanion contaminants from aqueous solution. *Carbon* 129:674–687. <https://doi.org/10.1016/j.carbon.2017.12.070>
- Liu C-H, Wu J-S, Chiu H-C, Suen S-Y, Chu KH (2007) Removal of anionic reactive dyes from water using anion exchange membranes as adsorbents. *Water Res* 41:1491–1500. <https://doi.org/10.1016/j.watres.2007.01.023>
- Liu X, Xiong X, Ding S, Jiang Q, Hu J (2017) Bi metal-modified Bi<sub>4</sub>O<sub>5</sub>I<sub>2</sub> hierarchical microspheres with oxygen vacancies for improved photocatalytic performance and mechanism insights. *Catal Sci Technol* 7:3580–3590. <https://doi.org/10.1039/c7cy01112a>
- Lu J, Chen Y, Li L, Cai X, Zhong S, Wu L, Chen J, Bai S (2019) Facet engineering on the interface of BiOCl–PbS heterostructures for enhanced broad-spectrum photocatalytic H<sub>2</sub> production. *Chem Eng J* 362:1–11. <https://doi.org/10.1016/j.cej.2018.12.130>
- Lyu H, Gao B, He F, Zimmerman AR, Ding C, Huang H, Tang J (2018) Effects of ball milling on the physicochemical and sorptive properties of biochar: experimental observations and governing mechanisms. *Environ Pollut* 233:54–63. <https://doi.org/10.1016/j.envpol.2017.10.037>
- Lyu H, Xia S, Tang J, Zhang Y, Gao B, Shen B (2020) Thiol-modified biochar synthesized by a facile ball-milling method for enhanced sorption of inorganic Hg<sup>2+</sup> and organic CH<sub>3</sub>Hg<sup>+</sup>. *J Hazard Mater* 384:121357. <https://doi.org/10.1016/j.jhazmat.2019.121357>
- Micheal K, Ayeshamariam A, Boddula R, Arunachalam P, AlSalhi MS, Theerthagiri J, Prasad S, Madhavan J, Al-Mayouf AM (2019) Assembled composite of hematite iron oxide on sponge-like BiOCl with enhanced photocatalytic activity. *Mater Sci Energy Technol* 2:104–111. <https://doi.org/10.1016/j.mset.2018.11.004>
- Mingke L, Hai L, Yin Hai B, Yingbo D, Liang W (2019) Efficient simultaneous removal of cadmium and arsenic in aqueous solution by titanium-modified ultrasonic biochar. *Bioresour Technol* 284:333–339. <https://doi.org/10.1016/j.biortech.2019.03.108>
- Mu'azu ND, Jarrah N, Kazeem TS, Zubair M, Al-Harhi M (2018) Bentonite-layered double hydroxide composite for enhanced aqueous adsorption of Eriochrome Black T. *Appl Clay Sci* 161:23–34. <https://doi.org/10.1016/j.clay.2018.04.009>
- Quan G, Fan Q, Cui L, Zimmerman AR, Wang H, Zhu Z, Gao B, Wu L, Yan J (2020) Simulated photocatalytic aging of biochar in soil ecosystem: insight into organic carbon release, surface physicochemical properties and cadmium sorption. *Environ Res* 183:109241. <https://doi.org/10.1016/j.envres.2020.109241>
- Rahman A, Urabe T, Kishimoto N (2013) Color removal of reactive dyes by clay adsorbents. *Procedia Environ Sci* 17:270–278. <https://doi.org/10.1016/j.proenv.2013.02.038>
- Sing KSW (1985) Reporting physisorption data for gas/solid systems with special reference to the determination of surface area and porosity (recommendations 1984). *Pure Appl Chem* 57:603–619. <https://doi.org/10.1351/pac198557040603>
- Sun J, Xu H, Li D, Zou Z, Wu Q, Liu G, Yang J, Sun L, Xia D (2018) Ultrasound-assisted synthesis of a feathery-shaped BiOCl with abundant oxygen vacancies and efficient visible-light photoactivity. *New J Chem* 42:19571–19577. <https://doi.org/10.1039/c8nj04165b>
- Tang J, Zhao B, Lyu H, Li D (2021) Development of a novel pyrite/biochar composite (BM-FeS<sub>2</sub>@BC) by ball milling for aqueous Cr(VI) removal and its mechanisms. *J Hazard Mater* 413:125415. <https://doi.org/10.1016/j.jhazmat.2021.125415>
- Wang S, Guan Y, Wang L, Zhao W, He H, Xiao J, Yang S, Sun C (2015) Fabrication of a novel bifunctional material of BiOI/Ag<sub>3</sub>VO<sub>4</sub> with high adsorption-photocatalysis for efficient treatment of dye wastewater. *Appl Catal B* 168:448–457. <https://doi.org/10.1016/j.apcatb.2014.12.047>
- Wang B, Gao B, Fang J (2017) Recent advances in engineered biochar productions and applications. *Crit Rev Environ Sci Technol* 47:2158–2207. <https://doi.org/10.1080/10643389.2017.1418580>
- Wang P, Zhang J, Shao Q, Wang G (2018) Physicochemical properties evolution of chars from palm kernel shell pyrolysis. *J Therm Anal Calorim* 133:1271–1280. <https://doi.org/10.1007/s10973-018-7185-z>
- Wu S, Xiong J, Sun J, Hood ZD, Zeng W, Yang Z, Gu L, Zhang X, Yang S-Z (2017) Hydroxyl-dependent evolution of oxygen vacancies enables the regeneration of BiOCl photocatalyst. *ACS Appl Mater Interfaces* 9:16620–16626. <https://doi.org/10.1021/acsami.7b01701>
- Yagub MT, Sen TK, Afroz S, Ang HM (2014) Dye and its removal from aqueous solution by adsorption: a review. *Adv Colloid Interface Sci* 209:172–184. <https://doi.org/10.1016/j.cis.2014.04.002>

- Yang X, Wan Y, Zheng Y, He F, Yu Z, Huang J, Wang H, Ok YS, Jiang Y, Gao B (2019) Surface functional groups of carbon-based adsorbents and their roles in the removal of heavy metals from aqueous solutions: a critical review. *Chem Eng J* 366:608–621. <https://doi.org/10.1016/j.cej.2019.02.119>
- Yang Z, Wang D, Zhang Y, Feng Z, Liu L, Wang W (2020) Photoreductive BiOCl ultrathin nanosheets for highly efficient photocatalytic color switching. *ACS Appl Mater Interfaces* 12:8604–8613. <https://doi.org/10.1021/acsami.9b22447>
- Yao Y, Gao B, Inyang M, Zimmerman AR, Cao X, Pullammanappallil P, Yang L (2011) Biochar derived from anaerobically digested sugar beet tailings: characterization and phosphate removal potential. *Bioresour Technol* 102:6273–6278. <https://doi.org/10.1016/j.biortech.2011.03.006>
- Zhang X, Gao B, Zheng Y, Hu X, Creamer AE, Annable MD, Li Y (2017) Biochar for volatile organic compound (VOC) removal: sorption performance and governing mechanisms. *J Bioresour Technol* 245:606–614. <https://doi.org/10.1016/j.biortech.2017.09.025>
- Zhang Y, Zuo S, Zhang Y, Ren G, Pan Y, Zhang Q, Zhou M (2019) Simultaneous removal of tetracycline and disinfection by a flow-through electro-peroxone process for reclamation from municipal secondary effluent. *J Hazard Mater* 368:771–777. <https://doi.org/10.1016/j.jhazmat.2019.02.005>
- Zhang J, Jiang C, Du Y, Sheng L, Huang X, Wang T, He J (2020) WO<sub>3</sub> rich in oxygen vacancies through ion-exchange reaction for enhanced electrocatalytic N<sub>2</sub> reduction to NH<sub>3</sub>. *ChemCatChem* 13:1146–1151. <https://doi.org/10.1002/cctc.202001769>
- Zhao S, Wen Y, Du C, Tang T, Kang D (2020) Introduction of vacancy capture mechanism into defective alumina microspheres for enhanced adsorption of organic dyes. *Chem Eng J* 402:126180. <https://doi.org/10.1016/j.cej.2020.126180>
- Zheng Y, Wan Y, Chen J, Chen H, Gao B (2020) MgO modified biochar produced through ball milling: a dual-functional adsorbent for removal of different contaminants. *Chemosphere* 243:125344. <https://doi.org/10.1016/j.chemosphere.2019.125344>
- Zubair M, Manzar MS, Mu'azu ND, Anil I, Al-Harhi MA (2020) Functionalized MgAl-layered hydroxide intercalated date-palm biochar for enhanced uptake of cationic dye: kinetics, isotherm and thermodynamic studies. *Appl Clay Sci* 190:105587. <https://doi.org/10.1016/j.clay.2020.105587>

## Authors and Affiliations

Yidan Luo<sup>1</sup> · Yonghu Wang<sup>1</sup> · Yaowei Zhu<sup>1</sup> · Mingshan Xue<sup>1</sup>  · Aofeng Zheng<sup>1</sup> · Yu Han<sup>1</sup> · Zuozhu Yin<sup>1</sup> · Zhen Hong<sup>1</sup> · Chan Xie<sup>1</sup> · Xibao Li<sup>1</sup> · Sheng Lei<sup>2</sup> · Bin Gao<sup>3</sup>

<sup>1</sup> Key Laboratory for Microstructural Control of Metallic Materials of Jiangxi Province, School of Materials Science and Engineering, Nanchang Hangkong University, Nanchang 330063, China

<sup>2</sup> School of Materials Engineering, Jiangsu University of Technology, Changzhou 213001, China

<sup>3</sup> Department of Agricultural and Biological Engineering, University of Florida, Gainesville, FL 32611, USA